NANOMATERIALS

Interfacial epitaxy of multilayer rhombohedral transition-metal dichalcogenide single crystals

Biao Qin[1,2]†, Chaojie Ma[1]†, Quanlin Guo[1]†, Xiuzhen Li[3]†, Wenya Wei[4], Chenjun Ma[1], Qinghe Wang[1], Fang Liu[1], Mengze Zhao[1], Guodong Xue[1], Jiajie Qi[1], Muhong Wu[5,6,7], Hao Hong[1,7], Luojun Du[3], Qing Zhao[1], Peng Gao[5], Xinqiang Wang[1], Enge Wang[5,6], Guangyu Zhang[3,6]*, Can Liu[2]*, Kaihui Liu[1,5,6]*

Rhombohedral-stacked transition-metal dichalcogenides (3R-TMDs), which are distinct from their hexagonal counterparts, exhibit higher carrier mobility, sliding ferroelectricity, and coherently enhanced nonlinear optical responses. However, surface epitaxial growth of large multilayer 3R-TMD single crystals is difficult. We report an interfacial epitaxy methodology for their growth of several compositions, including molybdenum disulfide (MoS_2), molybdenum diselenide, tungsten disulfide, tungsten diselenide, niobium disulfide, niobium diselenide, and molybdenum sulfoselenide. Feeding of metals and chalcogens continuously to the interface between a single-crystal Ni substrate and grown layers ensured consistent 3R stacking sequence and controlled thickness from a few to 15,000 layers. Comprehensive characterizations confirmed the large-scale uniformity, high crystallinity, and phase purity of these films. The as-grown 3R-MoS_2 exhibited room-temperature mobilities up to 155 and 190 square centimeters per volt second for bi- and trilayers, respectively. Optical difference frequency generation with thick 3R-MoS_2 showed markedly enhanced nonlinear response under a quasi–phase matching condition (five orders of magnitude greater than monolayers).

Two-dimensional (2D) transition-metal dichalcogenides (TMDs) are promising materials for ultrascaled transistors in next-generation electronic integrated circuits (ICs) and ultracompact components in photonic ICs (*1*–*6*). Theoretical analysis and experimental validation have consistently indicated that rhombohedral (3R) TMDs, compared to their monolayer and hexagonal (2H) counterparts, exhibit enhanced current density and higher carrier mobility (*7*, *8*), which makes them quite suitable for sub–5-nm node transistor channels (*9*–*11*). At the same time, the interlayer stacking manner of 3R-TMDs, which exhibits both broken in-plane inversion and out-of-plane mirror symmetries, enables switchable interfacial ferroelectricity (*12*–*15*), energy-efficient bulk photovoltaic effect (*16*–*18*), and constructive interference of nonlinear optical response (*19*–*22*).

The production of single-crystal 3R-TMDs has been limited because the growth of TMD layers on various substrates (including SiO_2/Si, sapphire, mica, glass, quartz, $SrTiO_3$, and Au) predominantly follows a surface epitaxy process (*23*–*31*). Under this growth mechanism, a new layer is grown on top of the existing layers, which intrinsically limits accurate control of the layer number or stacking phase because the interlayer interactions are quite weak (Fig. 1A). Although few-layer TMD films are accessible through layer-by-layer growth or direct bilayer nucleation on specific substrates (*32*, *33*), the surface proximity effect of the substrate quickly diminishes with increasing layer number. The influence of the surface energy from the substrate approaches almost zero when TMDs exceed two layers, and the thicker layer epitaxy becomes invalid (*34*). More notably, the minimal energy difference between the 3R and 2H phases (typically, 2H phases are ~1 to 10 meV/unit cell smaller than 3R ones) (*35*) leads to the coexistence of their turbostratic phases with predominantly 2H ones. Thus, surface epitaxial growth faces substantial challenges for the growth of 3R-TMD films on a large scale.

A notable example of the successful growth of 3R films was reported for rhombohedral BN, which was achieved by precipitating B and N atoms dissolved in Fe-Ni alloys (*36*). However, for TMDs, the situation becomes particularly complex because most metals tend to readily undergo chalcogenization and deterioration (an exception is Au, however, which primarily falls in the surface epitaxy of monolayers) (*37*). Here, we propose a universal strategy of interfacial epitaxy for producing wafer-scale 3R-TMD single crystals on Ni substrates alloyed with transition metals (denoted as Ni-M alloys). As illustrated in Fig. 1B, chalcogen atoms are gently released by breaking the surface dangling bonds of metal chalcogenides, which thereby prevents chalcogen-induced deterioration of the Ni-M metal. Thus, chalcogen atoms are sufficiently dissolved into the Ni-M substrate, followed by epitaxial precipitation of new layers at the substrate-existing layer interface. The activity of the interface is preserved by sequentially elevating as-formed layers, which drive the continuous epitaxy of multilayers. Meanwhile, the morphology of the metal stepped surface is maintained during the growth, which validates the unidirectional orientation of each layer (Fig. 1C and figs. S1 and S2). Theoretical calculations further show that the couplings between step edges and TMDs determine the orientation of each monolayer, whereas the interlayer couplings between TMD layers guarantee the pure 3R staking order to achieve single-crystal 3R-phase multilayers (fig. S3).

Interfacial epitaxy of 3R-MoS_2 single crystals

We take the 3R-MoS_2 multilayer single crystal as an illustrative example to demonstrate the interfacial epitaxy strategy. In our design, the transition metal Mo was first dissolved in single-crystal Ni(111) by annealing to form a Ni-Mo alloy substrate (figs. S4 and S5). Next, a metal chalcogenide plate of ZnS was placed beneath the alloy to provide a chalcogen source (Fig. 1B and fig. S6). At the optimized growth temperature, ZnS released S monomers (*38*) that could dissolve into the substrate. It prevents the accumulation of large S molecules on the metal surface, which otherwise will typically cause metal deterioration (fig. S7). The simultaneously dissolved sources were precipitated upward in the metal substrate, driven by both concentration and chemical potential gradient between the two surfaces of substrate. This led to the uninterrupted interfacial epitaxy of TMD multilayers, specifically in the 3R phase, guided by parallel steps on the metal substrate.

We used this strategy to grow multilayer 3R-MoS_2 single crystals. A photograph of a continuous MoS_2 film transferred onto a 2-inch (~5 cm) SiO_2/Si wafer (Fig. 2A) shows consistent optical contrast that is indicative of high film uniformity. Similar uniformity was observed in higher-magnification images (Fig. 2B and fig. S8) and Raman mappings of the A_{1g} mode of MoS_2 (fig. S9). The thickness of the MoS_2 film showed a near-linear dependence on the growth time within 5 hours, which allowed the layer number to be tuned from a few layers to ~15,000 layers (Fig. 2C and fig. S10). We estimated the growth rate to be ~50 layers min^{-1}, which surpasses conventional surface epitaxy because both Mo and S atoms were supplied efficiently at the interface.

The pronounced (003) peak in the x-ray diffraction (XRD) 2θ-scan data (Fig. 2D, top

[1]State Key Laboratory for Mesoscopic Physics, Frontiers Science Centre for Nano-optoelectronics, School of Physics, Peking University, Beijing, China. [2]Key Laboratory of Quantum State Construction and Manipulation (Ministry of Education), Department of Physics, Renmin University of China, Beijing, China. [3]Beijing National Laboratory for Condensed Matter Physics and Institute of Physics, Chinese Academy of Sciences, Beijing, China. [4]Guangdong Basic Research Center of Excellence for Structure and Fundamental Interactions of Matter, Guangdong Provincial Key Laboratory of Quantum Engineering and Quantum Materials, School of Physics, South China Normal University, Guangzhou, China. [5]International Centre for Quantum Materials, Collaborative Innovation Centre of Quantum Matter, Peking University, Beijing, China. [6]Songshan Lake Materials Laboratory, Dongguan, China. [7]Interdisciplinary Institute of Light-Element Quantum Materials and Research Centre for Light-Element Advanced Materials, Peking University, Beijing, China.
*Corresponding author. Email: canliu@ruc.edu.cn (C.L.); gyzhang@iphy.ac.cn (G.Z.); khliu@pku.edu.cn (K.L.)
†These authors contributed equally to this work.

panel) and three main peaks at intervals of exactly 120° in the φ-scan data (Fig. 2D, bottom panel) indicated that the as-grown MoS_2 film was well aligned without in-plane rotations. The uniform color in the electron backscatter diffraction (EBSD) inverse pole figure maps along both the Y- and Z-directions confirmed the single-crystalline nature of the film (Fig. 2E). Low-energy electron diffraction (LEED) patterns, measured at nine different positions, exhibited threefold symmetry and consistent alignment and further confirmed that the film was single crystalline on a wafer scale (Fig. 2F).

To investigate the stacking order of the as-grown MoS_2 single crystals, comprehensive characterizations with optical spectroscopy and electron microscopy were conducted. The six-lobed polarization-dependent second-harmonic generation (SHG) pattern revealed the preserved broken inversion symmetry of the as-grown film, indicative of a parallelly stacked 3R phase rather than a symmetric 2H phase (Fig. 2G and fig. S11). The uniform intensity in the SHG mapping of 3R-MoS_2 transferred onto a fused silica confirmed the consistent stacking sequence over a large area (Fig. 2H). The selected-area electron diffraction (SAED) pattern showed a near-zero peak intensity of the first-order diffraction representative of 3R-MoS_2 (Fig. 2I). Additionally, in-plane views of high-angle annular dark-field scanning transmission electron microscopy (HAADF-STEM) images revealed a triangular lattice, in which each atomic column represented a series of stacked Mo + S_2 with thickness-dependent intensities and a consistent contrast for thick layers (Fig. 2J and fig. S12) (*39*). The 3R stacking structure was further corroborated by the cross-sectional STEM images. The unit cell of the 3R phase was composed of three distinct layers. Each MoS_2 layer was aligned in the same direction, whereas the adjacent two layers slide by $a/\sqrt{3}$ along the in-plane armchair direction, where a is the lattice constant of MoS_2 (Fig. 2, K and L, and fig. S13). These results provided compelling evidence for the 3R stacking structure of our MoS_2 single crystals without the formation of 2H phases.

Universal growth of 3R-TMD single crystals

Our interfacial epitaxy methodology was also validated for the growth of various 3R-TMD materials. By modifying the transition metals (Mo, W, and Nb) and chalcogens (S and Se) dissolved into single-crystal Ni(111) substrates, diverse 3R-TMD films, including $MoSe_2$, WS_2, WSe_2, NbS_2, $NbSe_2$, and $MoS_{2(1-x)}Se_{2x}$ alloy, were successfully synthesized (Fig. 3A and fig. S14, A_1 to E_1; see materials and methods for more details). These TMD species were identified by their characteristic peaks in the XRD 2θ-scan spectra (Fig. 3I). The uniform contrast of the triangular lattice in the HAADF-STEM images (Fig. 3B and fig. S14, A_2 to E_2) and the near-zero intensity of the first-order diffraction spots in the SAED patterns (Fig. 3, C to H) demonstrate the achievability of their 3R phase by using our method. These studies confirm the universality, controllability, and scalability of our strategy for 3R-TMD single-crystal growth.

Electronic performance of 3R-MoS_2 thin layers

To assess the electronic properties of the 3R-MoS_2 single crystals, the as-grown films were transferred onto 20-nm–thick Al_2O_3/Si substrates to fabricate field-effect transistors (FETs) (fig. S15; see materials and methods for more details), with Ti/Au/Ti as the back-gate electrode and Sb as the contact (Fig. 4A). The output characteristics of a typical trilayer MoS_2 FET (channel length L_{ch} of 1 μm) are shown in Fig. 4B, which displayed a distinct *n*-type behavior and a high saturation current of 540 μA μm^{-1} under drain-source voltage V_{ds} = 3 V. The typical FET devices of mono-, bi-, and trilayer MoS_2 all maintained excellent electrostatic control, which confirmed the high quality of our samples obtained by the interfacial epitaxy strategy (Fig.

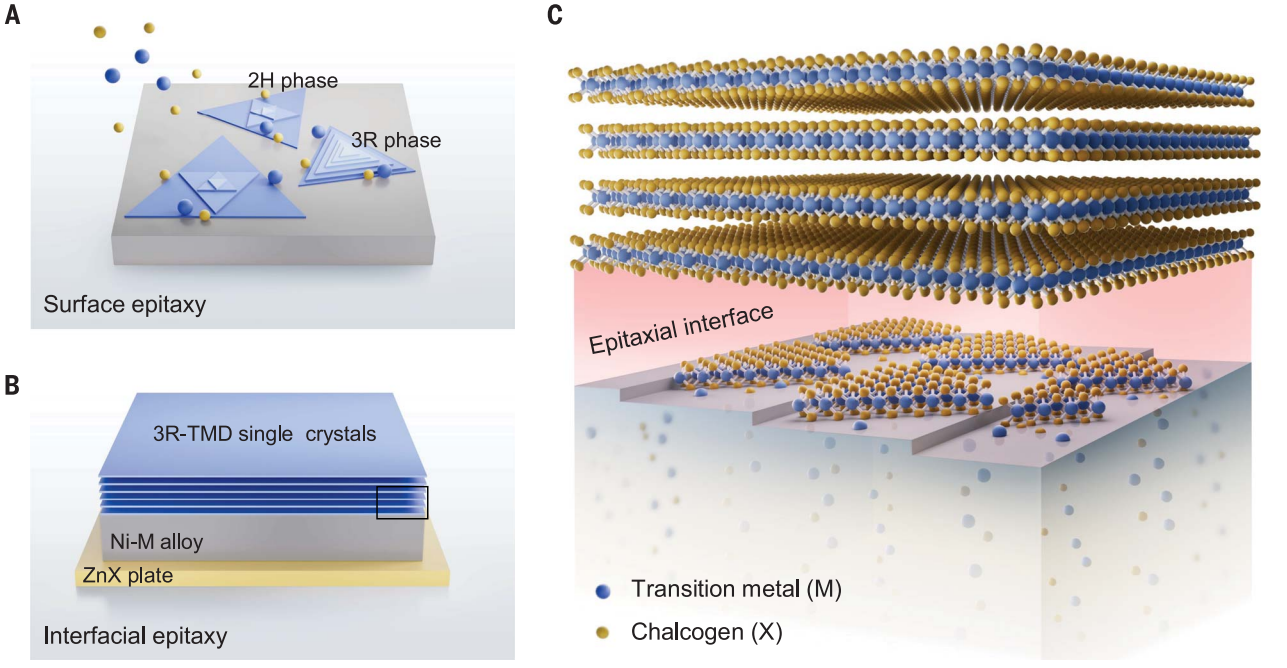

Fig. 1. Schematic illustrations for surface and interfacial epitaxy of 3R-TMDs. (**A**) Conventional surface epitaxy of multilayer TMDs. Precursors randomly nucleate on various substrates (such as SiO_2/Si, sapphire, mica, glass, quartz, $SrTiO_3$, and Au), which leads to simultaneous growth of both 2H- and 3R-phase polycrystalline TMDs. Neither the thickness nor the stacking order can be accurately controlled by the surface epitaxy strategy. (**B**) Interfacial epitaxy of 3R-TMD single crystals. A pre-annealed single-crystal Ni-M (M represents Mo, W, or Nb) alloy foil is placed on a ZnX (X represents S or Se) crystal plate, through which transition metal M and chalcogen X atoms are continuously supplied for 3R-TMD growth. (**C**) Zoomed-in diagram of the epitaxial interface in (B). The M and X atoms dissolved in the Ni substrate gradually precipitate at the epitaxial interface, wherein surface steps effectively guide the unidirectional orientation of each layer and form 3R-TMD single crystals. The thickness can be modulated from a few to ~15,000 layers with a consistent 3R stacking order.

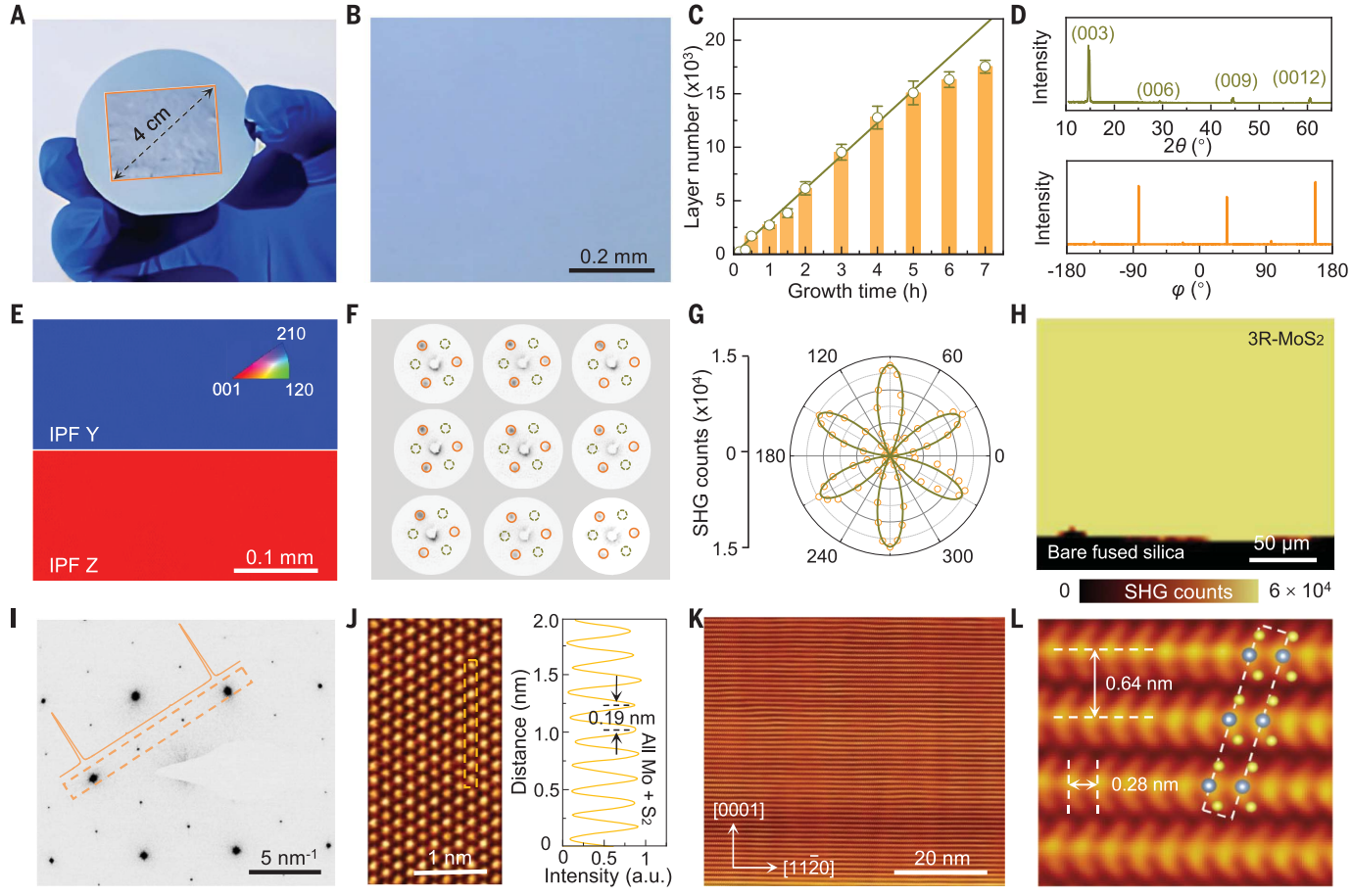

Fig. 2. Characterizations of 3R-MoS_2 multilayer single crystals. (**A**) Photograph of a 3R-MoS_2 single crystal on a 2-inch (~5-cm) SiO_2/Si wafer. (**B**) Optical image of the as-grown 3R-MoS_2 single crystal. (**C**) Layer number evolution of epitaxial MoS_2 single crystal with growth time. Error bars represent SDs from measurements of five samples. (**D**) XRD 2θ (top panel) and φ scan (bottom panel) of the 3R-MoS_2 film confirm the single-crystal nature of MoS_2 without in-plane rotation. (**E**) EBSD IPF-Y and IPF-Z maps of the 3R-MoS_2 film. (**F**) LEED patterns scanned across a 2-cm by 2-cm sample at nine different positions. The size of the electron beam is ~1 mm. (**G** and **H**) Polarized SHG pattern (G) and SHG mapping (H) of the 3R-MoS_2 film. (**I**) SAED pattern of the 3R-MoS_2 film with a layer number around 40. (**J**) HAADF-STEM image of the 3R-MoS_2 film with an intensity profile (right panel) along the orange dotted box (left panel). All the atom columns contain an equivalent number of atoms, that is, Mo+S_2, which confirms the 3R phase. a.u., arbitrary unit. (**K** and **L**) Cross-sectional HAADF-STEM image (K) and zoomed-in image (L) of 3R-MoS_2, which reveals the stacking order of the 3R phase.

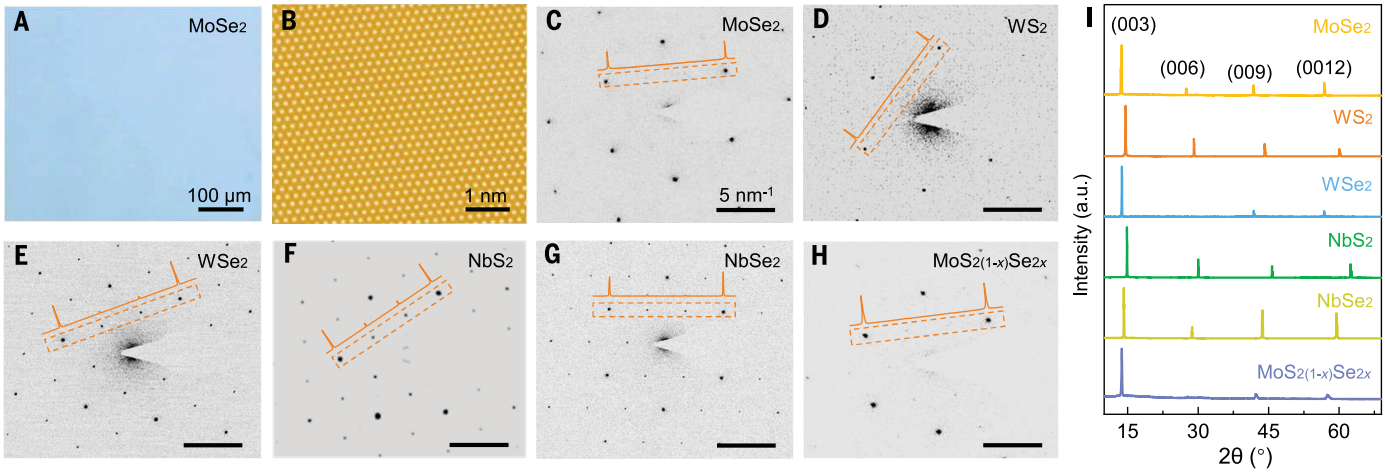

Fig. 3. Universal epitaxy of 3R-TMDs and their alloy single crystals. (**A** to **C**) Optical image (A), HAADF-STEM image (B), and SAED pattern (C) of 3R-$MoSe_2$ single crystals. (**D** to **H**) SAED patterns of 3R-WS_2 (D), 3R-WSe_2 (E), 3R-NbS_2 (F), 3R-$NbSe_2$ (G), and 3R-$MoS_{2(1-x)}Se_{2x}$ (H) single crystals. All images in (C) to (H) are of the same size. (**I**) XRD 2θ-scan spectra of 3R-TMD and their alloy single crystals. All the films are single crystals with an (003) facet index.

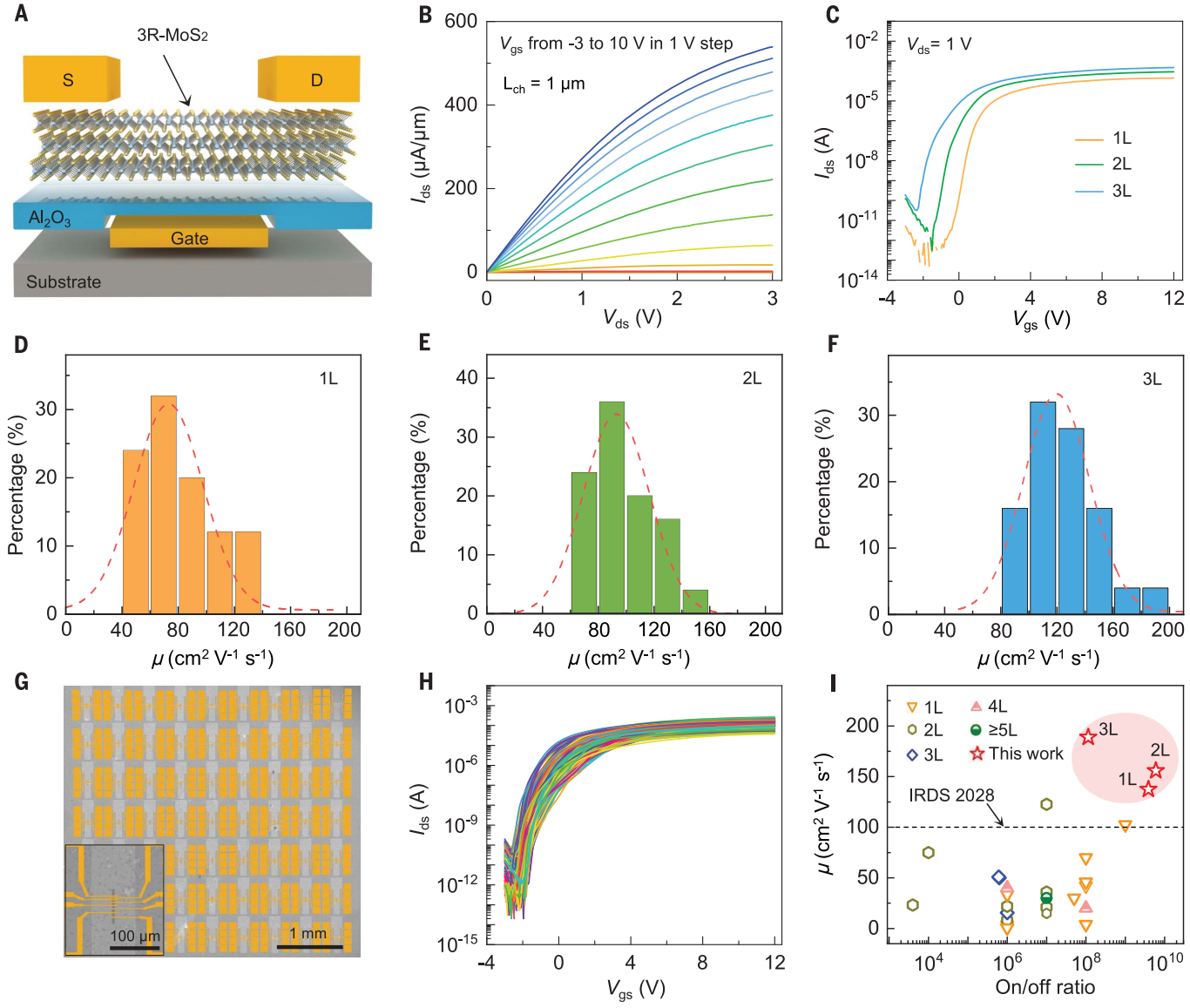

Fig. 4. Benchmark measurements of 3R-MoS_2 FETs. (**A**) Schematic of a backgated MoS_2 FET. (**B**) Output characteristic curves of the trilayer 3R-MoS_2 FET. V_{gs} ranges from −3 to 10 V with a 1-V step. Channel length (L_{ch}) is 1 μm. V_{gs}, gate-source voltage; I_{ds}, drain-source current. (**C**) Comparison of typical transfer characteristic curves of mono-, bi-, and trilayer MoS_2 FETs at V_{ds} = 1 V. (**D** to **F**) Mobility distributions of MoS_2 FETs based on mono- (D), bi- (E), and trilayers (F), respectively. The statistics show that the carrier mobility significantly increases with the layer number, with the highest values of 137, 155, and 190 $cm^2\ V^{-1}\ s^{-1}$ for mono-, bi-, and trilayers, respectively. The dashed line is a Gaussian fitting curve. (**G**) False-color scanning electron microscopy (SEM) image and a zoomed-in image (inset) of the backgated trilayer 3R-MoS_2 FET arrays. (**H**) Transfer characteristics of 100 trilayer 3R-MoS_2 FETs. (**I**) Comparison of the mobility and on/off ratio with previous works (materials and methods section S1.5). The dashed line denotes the mobility target in the IRDS 2028 roadmap (*40*).

4C). Notably, the trilayer 3R-TMDs exhibited an average carrier mobility of 120 $cm^2\ V^{-1}\ s^{-1}$, which is higher than that of the monolayers (73 $cm^2\ V^{-1}\ s^{-1}$) and bilayers (93 $cm^2\ V^{-1}\ s^{-1}$) (Fig. 4, D to F). This difference is believed to stem from their reduced Schottky barrier caused by the resistance to metal-induced Fermi-level pinning effect, as well as the slightly smaller bandgap of the 3R-MoS_2 few layers (*32*).

We fabricated ~400 devices (Fig. 4G), from which 100 transfer characteristic curves of trilayer 3R-MoS_2 FETs with varying positions and channel lengths were randomly selected (Fig. 4H). The device-to-device variations in the threshold voltage and on-state current were minimal, indicating the uniform electronic performance of the epitaxial 3R-MoS_2 films. Notably, the FET array devices demonstrate markedly high mobilities up to 137, 155, and 190 $cm^2\ V^{-1}\ s^{-1}$ for mono-, bi-, and trilayers, respectively (Fig. 4I). These values are similar to the highest values reported for intrinsic MoS_2 crystals and surpass the mobility target outlined in the International Roadmap for Devices and Systems (IRDS) (*40*). The benchmark testing of MoS_2 films, particularly the trilayers, shows that these films exhibit an exceptional current driving capability for large-scale ICs.

Nonlinear optical performance of 3R-MoS_2 thick layers

In addition to its electronic properties, 3R-MoS_2 with broken inversion symmetry displays enhanced nonlinear frequency conversion capabilities within a minimal footprint. The large nonlinear susceptibility $\chi^{(2)}$ of 100 to 1,000 pm V^{-1},

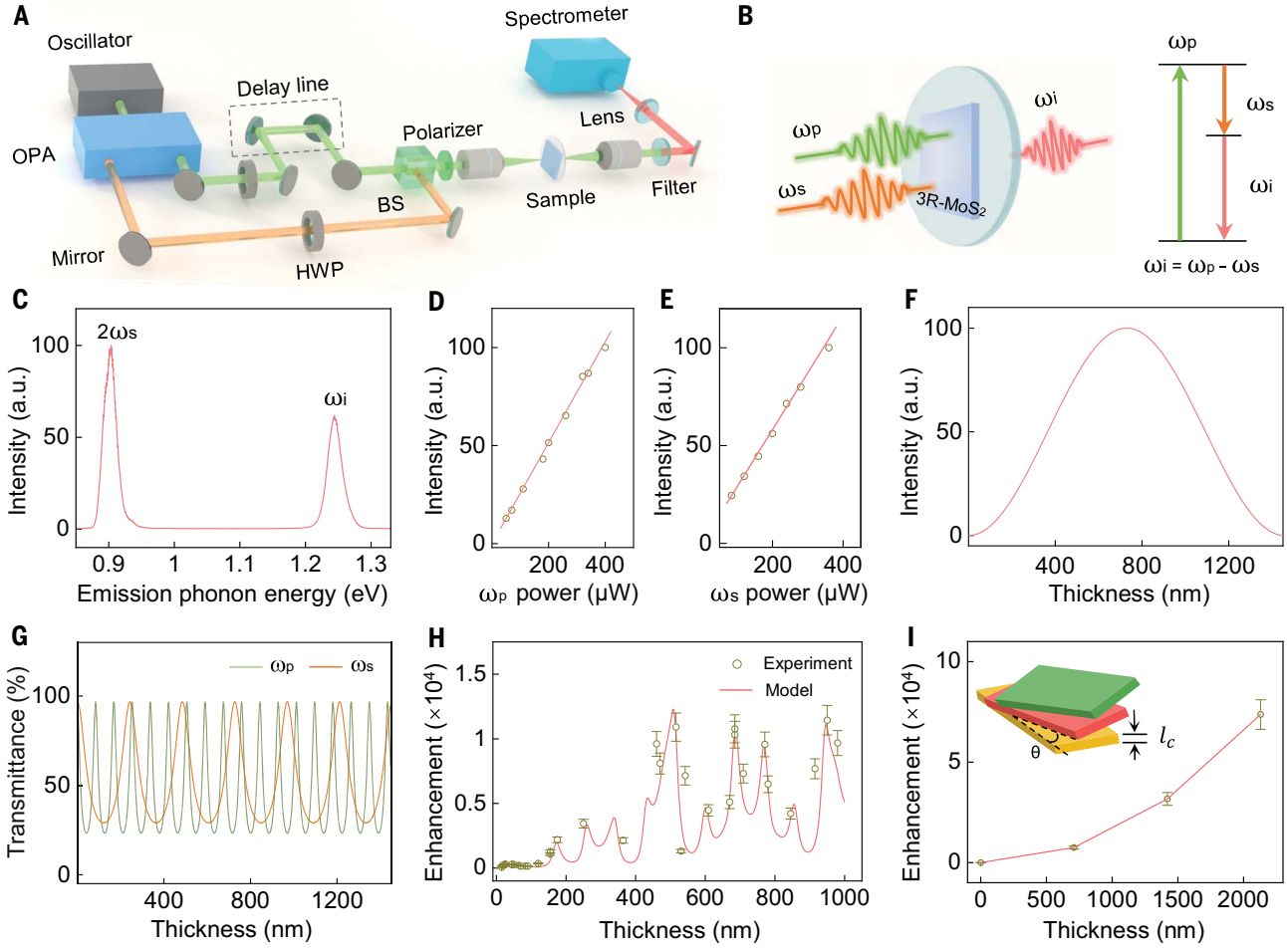

Fig. 5. DFG measurements of 3R-MoS_2 single crystals. (**A**) Sketch of the setup used for DFG experiments. BS, beam splitter; HWP, half-wave plate; OPA, optical parametric amplification. (**B**) Schematic of the DFG process for 3R-MoS_2. The pump photon ($\hbar\omega_p$) and signal photon ($\hbar\omega_s$) interact to generate the idler photon ($\hbar\omega_i$), following the law of energy conservation ($\omega_i = \omega_p - \omega_s$). (**C**) Spectrum measured during the DFG process for a thick 3R-MoS_2 crystal transferred onto fused silica. (**D** and **E**) Linear dependence of the idler intensity on the pump (D) and signal (E) powers. (**F**) Phase-mismatch curve of the DFG process calculated as a function of the 3R-MoS_2 thickness without considering multiple light reflections. (**G**) Calculated thickness-dependent transmissivity of 3R-MoS_2 for pump (green line) and signal (orange line) light. (**H**) Thickness-dependent idler enhancement of 3R-MoS_2 compared to the monolayer. The measured values are represented by dark yellow circles, and the theoretical predictions are indicated with the red line. (**I**) Quasi-phase matching in three twisted blocks of 3R-MoS_2. Each has a thickness of ~l_c and a twist angle of ~60° between them. Error bars represent SDs from multiple measurements.

which markedly surpasses that of conventional nonlinear optical crystals of 0.1 to 30 pm V^{-1}, and minimal absorption (nearly transparent above a wavelength of ~670 nm) make this material suitable for producing near-infrared light. In our experiment, the difference frequency generation (DFG, a second-order nonlinear optical process) of 3R-MoS_2 was measured with a transmission microscopic system (Fig. 5, A and B). The interaction between a pump photon $\hbar\omega_p$ (where $\hbar$ is Planck's constant divided by 2π and ω is the angular frequency) and a signal photon $\hbar\omega_s$ resulted in the creation of a low-energy photon, referred to as an idler photon ($\hbar\omega_i$) ($\omega_i = \omega_p - \omega_s$). When two pulsed laser beams, the pump at ~1.52 eV and the signal at ~0.62 eV, overlapped in space and were synchronized in time on the 3R-MoS_2 film, two peaks located at ~1.24 eV and ~0.90 eV were observed, which corresponded to the SHG of the signal and the DFG of the idler, respectively (Fig. 5C). The idler intensity linearly depended on both the pump and signal powers, as expected (Fig. 5, D and E).

The phase mismatching effect in DFG, which appeared as the sample thickness increased as a result of refractive index discrepancies among the pump, signal, and idler lights (*41*), theoretically caused the idler intensity to oscillate sinusoidally with the film thickness, with a peak at the coherence length l_c (Fig. 5F). However, the transmittance of both the pump and signal light varied periodically with the thickness because of multiple reflection effects (Fig. 5G), which led to a deviation from the expected sinusoidal oscillation of the idler intensity, and hence, a shift in the maximum idler intensity away from the coherence length of ~720 nm (Fig. 5H). To further enhance the DFG response, a quasi–phase matching strategy was adopted to compensate for the π-phase shift between adjacent 3R-MoS_2 thick layers (fig. S16). By stacking three blocks of 3R-MoS_2 thick layers (each with a thickness of ~l_c and a twist angle of ~60°), a nearly five orders of magnitude enhancement in the DFG was achieved compared with that of monolayer MoS_2 (Fig. 5I). The absolute DFG efficiency was calculated as ~60% W^{-1}, which is at least two orders of magnitude enhanced compared with conventional nonlinear crystals under a similar thickness

(*22*). This result demonstrated the feasibility of using 3R-TMDs as near-infrared nonlinear optical crystals that could be used for ultracompact integrated optical devices such as optical parametric amplification, optical parametric oscillation, and optical quantum circuits.

Discussion and outlook

The universal growth of wafer-scale, thickness-controlled 3R-TMD single crystals has been achieved through a nontrivial interfacial epitaxy strategy. The as-produced 3R-MoS_2 films were of high crystallinity, which enhanced the performance of FET arrays, including the high reproducibility and elevated mobility that exceeded the mobility benchmarks set by the IRDS. Additionally, we achieved near-infrared wavelength conversion and a notable nonlinear optical enhancement based on the thick 3R-TMD DFG process. We anticipate that these 3R-TMD single crystals will establish a versatile material platform for on-chip integration of 2D transistors and nonlinear optical devices. These advantages could move 3R-TMDs to forefront of technology in post–Moore's law nanoelectronics, nonvolatile memories, neuromorphic computing, solar energy harvesting, on-chip nonlinear optical devices, and quantum light sources.

REFERENCES AND NOTES

1. D. Akinwande *et al*., *Nature* **573**, 507–518 (2019).
2. Y. Liu *et al*., *Nature* **591**, 43–53 (2021).
3. K. C. Zhu *et al*., *Nat. Electron.* **4**, 775–785 (2021).
4. S. Das *et al*., *Nat. Electron.* **4**, 786–799 (2021).
5. Q. Guo *et al*., *Nature* **613**, 53–59 (2023).
6. M. Lee *et al*., *Science* **381**, 648–653 (2023).
7. X. Li *et al*., *Sci. Adv.* **9**, eade5706 (2023).
8. X. Zhang *et al*., *Nat. Commun.* **10**, 598 (2019).
9. T. Agarwal *et al*., *IEEE Trans. Electron Dev.* **62**, 4051–4056 (2015).
10. S. Das, H. Y. Chen, A. V. Penumatcha, J. Appenzeller, *Nano Lett.* **13**, 100–105 (2013).
11. S. L. Li *et al*., *Nano Lett.* **13**, 3546–3552 (2013).
12. S. Deb *et al*., *Nature* **612**, 465–469 (2022).
13. L. Rogée *et al*., *Science* **376**, 973–978 (2022).
14. X. Wang *et al*., *Nat. Nanotechnol.* **17**, 367–371 (2022).
15. A. Weston *et al*., *Nat. Nanotechnol.* **17**, 390–395 (2022).
16. Y. Dong *et al*., *Nat. Nanotechnol.* **18**, 36–41 (2023).
17. D. Y. Yang *et al*., *Nat. Photonics* **16**, 469–474 (2022).
18. J. Wu *et al*., *Sci. Adv.* **8**, eade3759 (2022).
19. M. Zhao *et al*., *Light Sci. Appl.* **5**, e16131–e16131 (2016).
20. J. Shi *et al*., *Adv. Mater.* **29**, 1701486 (2017).
21. A. Autere *et al*., *Adv. Mater.* **30**, e1705963 (2018).
22. X. Y. Xu *et al*., *Nat. Photonics* **16**, 698–706 (2022).
23. H. Zhu *et al*., *Nat. Nanotechnol.* **18**, 1295–1302 (2023).
24. J. H. Fu *et al*., *Nat. Nanotechnol.* **18**, 1289–1294 (2023).
25. K. S. Kim *et al*., *Nature* **614**, 88–94 (2023).
26. C. Gong *et al*., *ACS Nano* **7**, 11350–11357 (2013).
27. J. Zhu *et al*., *Nat. Nanotechnol.* **18**, 456–463 (2023).
28. J. Zhou *et al*., *Nature* **556**, 355–359 (2018).
29. C.-C. Huang *et al*., *ACS Appl. Mater. Interfaces* **14**, 42365–42373 (2022).
30. P. Chen, W. Xu, Y. Gao, J. H. Warner, M. R. Castell, *ACS Appl. Nano Mater.* **1**, 6976–6988 (2018).
31. P. Yang *et al*., *Nat. Commun.* **9**, 979 (2018).
32. L. Liu *et al*., *Nature* **605**, 69–75 (2022).
33. Q. Wang *et al*., *Natl. Sci. Rev.* **9**, nwac077 (2022).
34. L. Zhang, J. Dong, F. Ding, *Chem. Rev.* **121**, 6321–6372 (2021).
35. J. G. He, K. Hummer, C. Franchini, *Phys. Rev. B Condens. Matter Mater. Phys.* **89**, 075409 (2014).
36. J. Qi *et al*., *Adv. Mater.* **36**, e2303122 (2024).
37. Y. Gao *et al*., *Nat. Commun.* **6**, 8569 (2015).
38. Y. Zuo *et al*., *Nat. Commun.* **13**, 1007 (2022).
39. X. Zhao, S. Ning, W. Fu, S. J. Pennycook, K. P. Loh, *Adv. Mater.* **30**, e1802397 (2018).
40. *International Roadmap for Devices and Systems 2021 Edition* (IEEE, 2021); https://irds.ieee.org/.
41. Y. R. Shen, *The Principles of Nonlinear Optics* (Wiley, 1984).

ACKNOWLEDGMENTS

Funding: This work was supported by the National Natural Science Foundation of China (grant nos. 52025023, 52322205, 52250398, 12274456, 51991342, 92163206, 11888101, and 62305003), National Key R&D Program of China (grant nos. 2022YFA1403500, 2022YFA1405600, and 2021YFA1400502), Guangdong Major Project of Basic and Applied Basic Research (grant no. 2021B0301030002), Beijing Municipal Science and Technology Project (grant no. Z221100005822003), and the Strategic Priority Research Program of Chinese Academy of Sciences (grants no. XDB33000000 and XDB43000000). This work has been supported by the New Cornerstone Science Foundation through the XPLORER PRIZE. We thank the National Supercomputer Centre in Tianjin for computing support. **Author contributions:** K.L., C.L., and G.Z. supervised the project. K.L. and C.L. conceived the experiments. B.Q., C.L., and K.L. developed the growth mechanism. B.Q. conducted the growth experiments. Chaojie Ma, W.W., Chenjun Ma, H.H., and K.L. performed the theoretical calculations and the DFG experiments. X.L., B.Q., L.D., and G.Z. performed the electrical measurements. B.Q., M.Z., and H.H. performed the SHG measurements. Q.G., B.Q., and P.G. performed the transfer of TMDs and the TEM experiments. B.Q., J.Q., Q.W., G.X., M.W., F.L., and X.W. performed the Raman, LEED, SEM, EBSD and XRD experiments. B.Q., Chaojie Ma, Q.G., X.L., K.L., and C.L. wrote the article. L.D., Q.Z., G.Z., and E.W. revised the manuscript. All the authors discussed the results and revised the paper. **Competing interests:** The Peking University has filed a Chinese patent application (202410325437.6) with K.L., C.L., and B.Q. listed as inventors. **Data and materials availability:** All data are available in the main text or the supplementary materials.

SUPPLEMENTARY MATERIALS

science.org/doi/10.1126/science.ado6038
Materials and Methods
Figs. S1 to S16
References (*42*–*62*)

Submitted 13 February 2024; accepted 17 May 2024
10.1126/science.ado6038